Applications in Engineering Science 19 (2024) 100190

Contents lists available at ScienceDirect

Applications in Engineering Science

journal homepage: www.elsevier.com/locate/apples

Dynamic origami solar eyes with tensegrity architecture for energy harvesting Mashrabiyas

Fernando Fraternali [a,*], Enrico Babilio [b], Rana Nazifi Charandabi [c], Giovanni Germano [a], Raimondo Luciano [d], Giovanni Spagnuolo [c]

[a] Department of Civil Engineering, University of Salerno, Fisciano (SA), 84084, Italy
[b] Department of Structures for Engineering and Architecture (DiSt), University of Naples "Federico II", Naples, 80134, Italy
[c] Department of Information Engineering, Electrical Engineering and Applied Mathematics (DIEM), University of Salerno, Fisciano (SA), 84084, Italy
[d] Department of Engineering, University of Naples "Parthenope", Naples, 80143, Italy

ARTICLE INFO

Keywords:
Mashrabiya
Origami
Tensegrity
Photovoltaics
Solar energy

ABSTRACT

Mashrabiya are oriel windows characteristic of Islamic architectural tradition that were historically integrated into buildings located in places with arid climates. The present paper formulates a novel design approach to Mashrabiya systems, by employing origami modules equipped with photovoltaic cells. The examined oriel window is able to complement the main traditional functions of a Mashrabiya with solar energy harvesting. A primary folding motion of the origami modules designed to tessellate its surface permits the sunlight to pass through the system in a controlled way. A secondary tilting folding motion of the photovoltaic cells placed on these modules lets the system harvest solar energy and produce electric power. The paper illustrates the architectural and mechanical design of the examined Mashrabiya window, as well as its energy harvesting properties, using both numerical and experimental methods.

1. Introduction

The increasing growth of population and migration from rural areas to cities has severely impacted the demand for electric power, nowadays still mainly generated from fossil fuels. Economically growing countries located in arid climates, such as, e.g., Saudi Arabia, the United Arab Emirates, the southern part of Iran, and several other countries in the Middle East, are particularly affected by such a phenomenon, contributing to soaring electricityprices (Taki and Kumari, 2023). The Mashrabiya is a 'vernacular' element of the architectural heritage of Islamic countries. It consists of a veranda covered on three sides by a wooden lattice with variable motifs and lattice spacing (see, e.g., Fathy (1986), Giovannini et al. (2015), Karamata and Andersen (2014) and Taki and Kumari (2023)). It offers several advantages over porch systems, especially in buildings located in arid climates. Those essentially consist of the capacity of the Mashrabiya to transform direct light into diffuse light, due to the employment of rich latticework with round balusters, small lattice spacing in the bottom part and larger lattice spacing above eye level, useful also for privacy reasons. Mashrabiya windows are also able to create a beneficial airflow circulation in the inner spaces of a building, with controlled humidity and temperature (Fathy, 1986). This humidified airflow is produced by the entry of cool air through the bottom section of the Mashrabiya lattice, the exit of hot air through the top section, and the use of water pots placed behind the lattice as evaporative coolers. Mashrabiya systems therefore qualify as architectural elements that produce thermal and humidity comfort, well-being and privacy in the inner spaces of a building, through the use of fully environmentally-sustainable techniques. Unfortunately, over the last years Mashrabiya windows have been progressively replaced by modern and more easy-to-manufacture windows and porch systems in Middle-Eastern countries (Taki and Kumari, 2023). Nevertheless, shape-varying, modern designs of Mashrabiyas have recently been proposed in the literature (Giovannini et al., 2015; Karamata and Andersen, 2014), making use of perforated opaque shields that can produce relative horizontal and vertical motions.

Merging the two concepts of the Mashrabiya and photovoltaic (PV) cells awaits attention. PV cells are increasingly used in energy efficient buildings to form dynamic, sun-tracking windows that combine daylight shading with electric power generation (refer, e.g., to Gao et al. (2018) and Vassiliades et al. (2022)). Nowadays, PV modules can be classified into three different generations, encompassing crystalline, amorphous, inorganic and organic cells with various average visible-light transmission (AVT) properties and power conversion efficiencies (PCE) (Lu et al., 2022; Gorjian et al., 2022). Beside the

* Corresponding author.
E-mail address: f.fraternali@unisa.it (F. Fraternali).

https://doi.org/10.1016/j.apples.2024.100190
Received 17 July 2024; Accepted 8 August 2024
Available online 13 August 2024

Nomenclature

α	Vertex angle of the generic macro-triangle (rad)
γ	Angle between the normal to the PV panel and the sun ray vector (rad)
η	Power conversion efficiency (PCE) of a PV module
ξ	Variable describing the kinematics of the primary folding motion ($\xi \in [0, 1]$)
$\dot{\xi}$	Primary folding motion pseudo-velocity (s^{-1})
θ_i	Tilting angle of the ith micro-triangle (rad or deg; $i = 1, 2, 3$)
$\dot{\theta}_i$	Secondary folding motion pseudo-velocity ($rad\,s^{-1}$)
ψ_s, φ_s, ζ_s	Solar azimuth, elevation and zenith angles (deg)
$\triangle$	Micro-triangle symbol
$\mathbf{e}_i$	ith unit vector of the Cartesian frame of reference ($i = 1, 2, 3$)
E_{act}	Activation energy of the solar eye module (W h)
$E_{PV,m}$	Energy harvested by a solar eye module (W h)
E_{TW}	Net electrical energy produced by a TMas window (kW h)
E_{TF}	Net electrical energy produced by a TMas façade (kW h/m^2)
$I_{b,n}$	Direct normal irradiance (DNI; Wm^{-2})
L	Characteristic length of the generic macro-triangle (mm)
$\mathbf{n}_i$	Unit vector normal to the ith panel ($i = 1, \ldots, 8$)
$\mathbf{n}_s$	Sun ray unit vector
$P^{\triangle}_{b,in}$	Input power on a single micro-triangle (W)
P_{in}	Total input power on the solar eye module (W)
P_{out}	Total output power on the solar eye module (W)
$P_{act,i}$	Activation power for primary ($i = 1$) and secondary ($i = 2$) folding motions (mW)
$\mathbf{R}$, $\mathbf{R}''$	Rotation tensors
S_b	Direct-beam-illuminated area on a micro-triangle (m^2)
Δt	Time step (s)
$T_{act,i}$	Total activation time for primary ($i = 1$) and secondary ($i = 2$) folding motions (s)
UTC	Coordinated Universal Time
$\mathbf{X}_i$, $\mathbf{x}_i$, $\mathbf{y}_i$	Position vectors of the nodes of a macro-triangle (mm; $i = 0, \ldots, 3$)

first-generation crystalline and opaque PV cells, amorphous modules and organic solar cells have been respectively developed in second- and third-generation systems, among others (refer, e.g., to the detailed classification presented by Lu et al. (2022)). Particularly interesting is the category of organic photovoltaics (OPV), which have the ability to selectively absorb the sunlight in the near-infrared and the ultraviolet regions of the electromagnetic spectrum, permitting instead visible-light transmission (Burgues-Ceballos et al., 2021). OPV cells can be usefully employed in building integration (Song et al., 2023), while semi-transparent organic photovoltaic (ST-OPV) modules are diffusely employed in agrivoltaic applications, mainly to form PV greenhouses (PVG) (Gorjian et al., 2022; Lu et al., 2022; Fernández et al., 2022; Moshari et al., 2023). The PCE of such systems varies from the 27%–29% of opaque crystalline silicon and amorphous gallium arsenide cells, respectively, down to the 18%–20% of opaque colored panels (see, e.g., FuturaSun® (2024)); the 9%–12% of semi-transparent solar cells with AVT in the range 60 to 77%, and the 4 to 5% of OPV modules with 60 to 65% AVT (Gorjian et al., 2022).

This paper presents the concept and the main technical features of innovative, tensegrity Mashrabiyas (TMas), engineered to provide a modern and energetically convenient reformulation of traditional Mashrabiya systems. Such oriel windows make use of deployable tensegrity-origami structures and are equipped with sun-tracking arrays of PV cells for solar energy harvesting (Fraternali et al., 2024). The solar eyes analyzed in this study are formed by four 'macro-triangles', each of which is in turn composed of two 'micro-triangles'. A primary activation motion of the system produces the folding of the micro-triangles out-of-plane, thus inducing a suitable penetration of the light into the inner spaces, with the aim of realizing the desired shading ratio, depending on the season and the time of the day. A secondary motion is superimposed onto the primary one, with the aim of optimally tilting the PV micro-triangles to maximize their solar energy harvesting capacity. The geometry of the tensegrity structure forming the TMas module is inspired by a Mashrabiya pattern, which dynamically changes shape due to the folding of the solar eyes. This element can be conveniently employed to form solar façades equipped with shading devices and photovoltaic windows featuring various textures (Attoye et al., 2017; Vassiliades et al., 2022; Gao et al., 2018). The use of mosaic-type PV cells (Ebert et al., 2016; Mittag et al., 2018) or OPV modules (Song et al., 2023) means PV patterns can be achieved which reproduce, e.g., a variety of Islamic geometric designs (Bonner, 2016), thus adding additional aesthetic value to the TMas. The paper includes a technical description of the employed solar eyes (Section 2), as well as the architectural design of a TMas window (Section 3). The estimation of the energy harvesting capacity of TMas elements is presented in Section 5. Concluding remarks and directions for future work are finally presented in Section 6.

2. Origami solar eyes

The origami solar eye modules that form the TMas have a quadrangular shape and are composed of four foldable macro-triangles, each made of two micro-triangles covered with PV cells (Fig. 1). Top and axonometric views of three configurations achieved by a single solar eye module during the primary folding motion are shown in Fig. 1(A), while Fig. 1(B) illustrates an animation of the tilting motion of a micro-triangle, which is superimposed onto the primary motion. The dimensions of the generic macro-triangle forming the solar eye analyzed in the present work are illustrated in Fig. 1(C).

A physical model of such a device, which has a footprint of about 29 cm, has been built making use of 3D printing techniques and the manual assembly of additional parts, as described in Fraternali et al. (2024). In the model built-up for the study presented in Fraternali et al. (2024), each micro-triangle is covered with six 25 mm×30 mm mini PV cells provided by AliExpress® (https://www.aliexpress.com/). The study presented in Section 5.1 refers to a different arrangement of PV cells, which employs a single, custom-made array of mini PV cells on each single micro-triangle, giving a total of 8 PV arrays for the overall solar eye module. The physical model is equipped with a DC motor that drives the primary folding motion (voltage of 12 V; rotational speed of 15 rpm), through the change of the rest length of a bus cable running along the perimeter of the unit cell, as shown in Fig. 1(A). By increasing or decreasing the rest length, the motor produces a sliding motion of four rollers against diagonal linear guides. Additional DC motors (voltage of 12 V; rotational speed of 16 rpm) rotate small winches attached to bars with half-moon cross sections, which are placed underneath

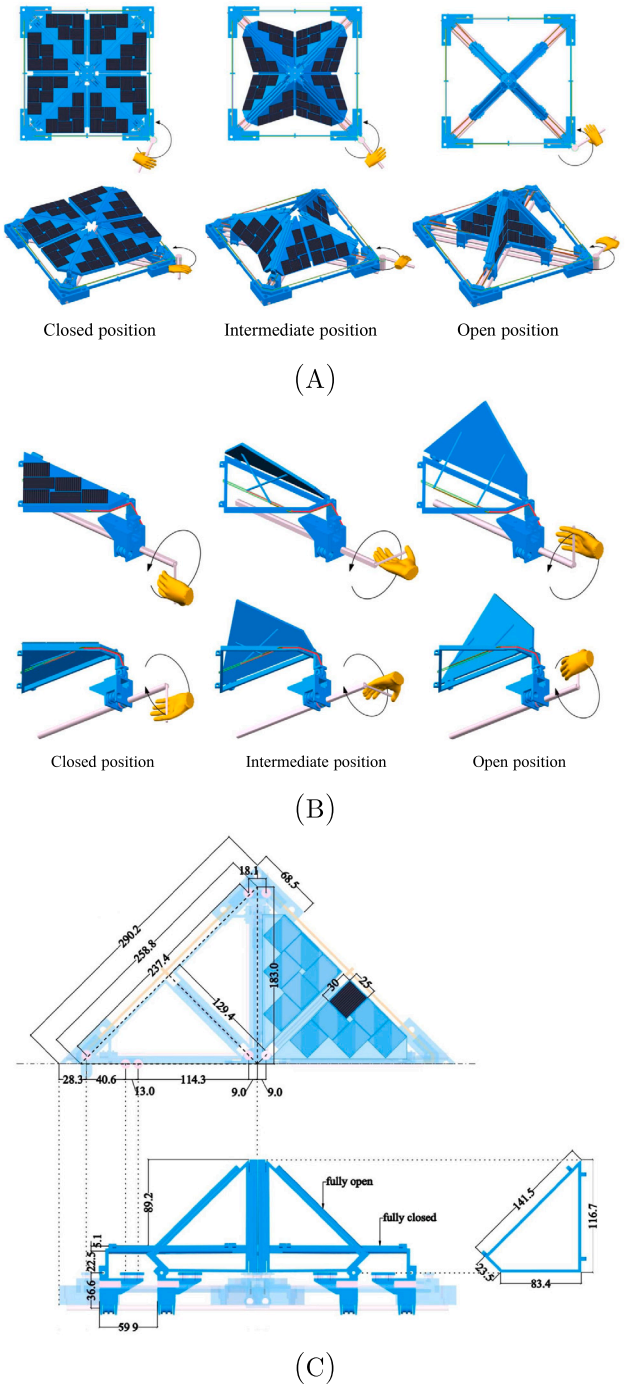

Fig. 1. Opening and closing mechanisms of the primary (A) and secondary (B) folding motions of the quadrilateral solar eye module. (C) Dimensions in mm of the solar eye unit cell.
Source: Reproduced from Supplementary Text of Fraternali et al. (2024) under CC 4.0 license.

the guides of the primary motion. This secondary motion produces the change of the rest lengths of bus cables connected to scissor tensegrity structures, which smoothly tilt the micro-triangles forming the system, as shown in Fig. 1(B). An analytic description of the kinematics of the solar eyes is given in Section 5.1. The reader is referred to Fraternali et al. (2024) for additional details about the fabrication methods and the mechanics of this tensegrity-origami module.

3. Architectural design of a TMas oriel window

Let us design a TMas prismatic oriel window that tessellates origami solar eyes on four faces: front face, two lateral faces and top face. As illustrated in Fig. 2, the designed TMas window includes 24 solar eye units on the front face; 16 units on each of the two lateral faces and 8 units on the top face, which gives a total of 64 units (we have counted a module formed by four micro-triangles as half a unit). The solar eye units are mounted on perforated timber panels with holes reproducing a Mashrabiya pattern. The employed pattern features fine scale holes on the bottom portions of the timber panels (for privacy reasons), and larger scale holes on the top portions (to favor air circulation on the back of the panel, from bottom to top) (Fathy, 1986). The activation motors of the solar eye units are placed on the back of the junction elements of the timber panels. At a junction that does not lie on the perimeter of the generic panel, we place one motor to drive the primary folding of one unit converging to the junction (e.g., the one to the left of the junction), plus eight additional motors driving the secondary (tilting) folding motions of the eight micro-triangles that converge at the junction. A smaller number of motors are placed behind the perimeter junctions, depending on the number of units attached to the junction.

As anticipated, the PV cells covering the micro-triangles of the solar eyes are assumed to be custom-made so as that we can employ a single cell for each micro-triangle (see also Section 5.1). In the present work, we decide to use opaque, Silk® Nova Red cells with 18.97% PCE (FuturaSun®, 2024), addressing the employment of mosaic-type PV cells (Ebert et al., 2016; Mittag et al., 2018) and/or OPV modules (Song et al., 2023) to future studies. Fig. 3 shows an animation of the opening (primary) folding motion of the solar eyes forming the TMas window, which permit, in a controlled way, the penetration of the sunlight into the inner spaces of the building served by the window. We will describe in Section 5.1 an optimized strategy to activate the primary and secondary folding motions of the generic solar eye, driven by a sun-tracking algorithm. It is also possible to drive these motions according to an alternative strategy, with the aim of optimizing the shading ratio of the window and the transformation of direct sunlight into diffuse light (Giovannini et al., 2015; Karamata and Andersen, 2014). Eventually, the two strategies above can be combined into a multi-objective (sun-tracking/shading) optimization strategy, which we plan to study through future research.

4. Kinematics

This section presents the key aspects of the kinematics of the solar eye module, diffusely illustrated in Fraternali et al. (2024). Let us refer to a macro-triangle forming such a system, by using the symbols $\mathbf{X}_i$, $\mathbf{x}_i$ and $\mathbf{y}_i$ $(i = 0, 1, 2, 3)$ to denote the position vectors of its nodes in the fully flat configuration, the configuration produced by the primary folding motion and the configuration produced by the secondary folding motion, respectively (Fig. 4).

The primary folding motion is described by the following vector equations (Babilio et al., 2019)

$$\mathbf{x}_0 = \mathbf{X}_0 + a_0 L \mathbf{e}_3 \,, \tag{1}$$

$$\mathbf{x}_1 = \mathbf{X}_1 - a_1 L \mathbf{e}_1 \,, \tag{2}$$

$$\mathbf{x}_2 = \mathbf{X}_2 - a_2 L \left(\cos \frac{\alpha}{2} \mathbf{e}_1 + \sin \frac{\alpha}{2} \mathbf{e}_2 \right) - a_3 L \mathbf{e}_3 \,, \tag{3}$$

$$\mathbf{x}_3 = \mathbf{R}_\alpha \mathbf{x}_1 \,, \tag{4}$$

where $\alpha = \pi/2$ denotes the angle formed by the segments $\mathbf{X}_1 - \mathbf{X}_0$ and $\mathbf{X}_3 - \mathbf{X}_0$ in the fully flat configuration; $L = 183$ mm denotes the lengths of these segments (Fig. 1); $\mathbf{e}_1$ is the unit vector in the direction of $\mathbf{X}_1 - \mathbf{X}_0$; $\mathbf{e}_2$ is the unit vector in the direction of $\mathbf{X}_3 - \mathbf{X}_0$; $\mathbf{e}_3$ is the unit vector

Fig. 2. Different views of a TMas oriel window having the solar eye modules in closed position: axonometric view (A), front-view (B), top-view (C), and side-view (D).

orthogonal to the plane of the fully folded configuration; and it results in

$$\mathbf{R}(\alpha) := \cos\alpha\,(\mathbf{e}_1\otimes\mathbf{e}_1+\mathbf{e}_2\otimes\mathbf{e}_2) + \sin\alpha\,(\mathbf{e}_2\otimes\mathbf{e}_1-\mathbf{e}_1\otimes\mathbf{e}_2)+\mathbf{e}_3\otimes\mathbf{e}_3, \tag{5}$$

$$a_0 = \sqrt{\varepsilon\,(2-\varepsilon)}\,, \tag{6}$$

$$a_1 = \varepsilon\,, \tag{7}$$

$$a_2 = \frac{\varepsilon}{2}\,\frac{\sin\alpha+2\cos\frac{\alpha}{2}}{1-(1-\varepsilon)\sin\frac{\alpha}{2}}\,, \tag{8}$$

$$a_3 = \sqrt{\varepsilon\,(2-\varepsilon)}\,\sin\frac{\alpha}{2}\,\frac{1-\varepsilon-\sin\frac{\alpha}{2}}{1-(1-\varepsilon)\sin\frac{\alpha}{2}}\,. \tag{9}$$

Here, ε indicates the control variable defined through

$$L_{13}(1-\varepsilon) = \ell_{13}\,, \tag{10}$$

L_{13} and ℓ_{13} denoting the lengths of the segments $\mathbf{X}_3-\mathbf{X}_1$ and $\mathbf{x}_3-\mathbf{x}_1$, respectively. By changing the rest length of the bus cable that runs along the perimeter of the fully flat configuration of the solar eye, one suitably changes the value of ε and folds the macro-triangle out-of-plane. The maximum value of ε is equal to $1-\sqrt{2}/2$ and is attained in the fully folded configuration, when the out-of-plane displacement of the vertex $\mathbf{X}_0$ is equal to $\sqrt{2}/2L = 129$ mm.

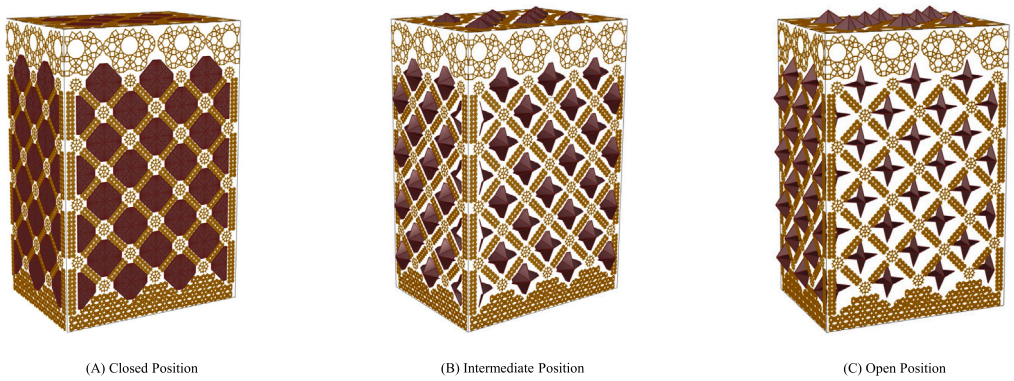

Fig. 3. Animation of the opening mechanism of the solar eye modules forming the TMas window.

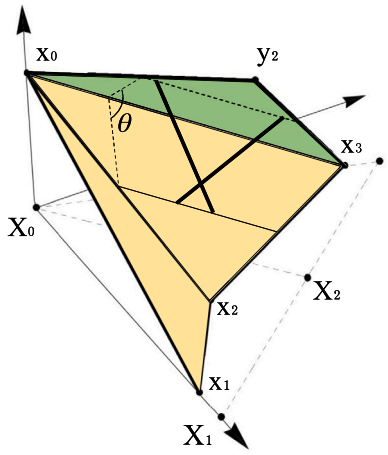

Fig. 4. Illustration of the kinematics of a macro-triangle forming the solar eye module.

We now move on to describe the kinematics of the (secondary) tilting motion of the micro-triangle with vertices $\mathbf{x}_0$, $\mathbf{x}_2$ and $\mathbf{x}_3$, obtaining (Fraternali et al., 2024)

$$\mathbf{y}_i = \mathbf{R}''\mathbf{x}_i \tag{11}$$

where $\mathbf{R}''$ is a rotation matrix of an angle θ about the axis $\mathbf{x}_3 - \mathbf{x}_0$. One changes the tilting angle θ by varying the rest length of a bus cable running in the plane $\mathbf{x}_0$, $\mathbf{x}_2$, $\mathbf{x}_3$. This cable is connected to a tensegrity scissor structure that finely tunes the rotation $\mathbf{R}''$ (Fig. 4). The maximum (theoretical) tilting angle of the examined physical model is equal to 94 deg: it is reached when the bars forming the scissor structure are parallel to each other, as described in Fraternali et al. (2024) (see Fig. 13 in this reference). The folding motion of the micro-triangle with vertices $\mathbf{x}_0$, $\mathbf{x}_2$ and $\mathbf{x}_1$ is described in a similar way, by introducing a new tilting angle. Overall, the kinematics of the solar eye is designed with nine controls variables: the scalar variable $\xi = (2 + \sqrt{2})\varepsilon \in [0, 1]$, and the eight tilting angles $\theta_1, \ldots, \theta_8$ of the micro-triangles forming the module (Fig. 1).

5. Estimation of produced and demanded energies

We estimate hereafter the electric energy that is harvested by a single solar eye module installed on a Mashrabiya element (Section 5.1), and the energy required to activate the primary and secondary folding motions of such a module. (Section 5.2).

5.1. Harvested solar energy

A first study of the solar energy harvesting capacity of a solar eye module is conducted with reference to a Mashrabiya window installed on a vertical façade facing south, within a building located in the city of Tunis, Tunisia. The examined site is identified by the decimal geographic coordinates 36.796 639 976 latitude and 10.171 966 553 longitude. We assemble data about the sun path and the direct solar irradiance (DNI) in the Tunis site, for selected days of the year, making use of PVLib v0.10.3, a Python toolbox that has been developed for simulating the performance of photovoltaic energy systems (Holmgren et al., 2023). Our analysis focusses on the summer and winter solstices of the year 2023, which are the longest (June 21) and the shortest (December 21) days of the year, respectively, as well as the spring and autumn equinoxes of the year 2023 (March 20 and September 23, respectively), that is, the days in which day and night have equal duration, due to the fact that the sun is exactly above the equator. Fig. 5 shows predictions for the sun paths, the azimuth angle ψ_s (measured from the north), the elevation angle φ_s, and the complementary of the elevation angle, i.e. the zenith angle ζ_s, on the selected days.

Inspecting Fig. 5(C), one observes that the sun path remains in the southern sky the entire day during the winter solstice and the equinoxes (green and orange curves, respectively). In contrast, at the summer solstice the sun rises north east and sets north west, crossing into the southern sky at around 9 AM and crossing back into the northern sky at around 4 PM. This implies that a building façade facing south, when free from shadowing bodies (such as mountains, trees, or other buildings), will be lit from sunrise to sunset at the winter solstice and equinoxes. Differently, the same façade will be illuminated by the sun only for part of the summer solstice, as shown in Fig. 6(A). In this figure, the number of hours per day during which a south facing façade receives direct sunlight (red-colored curve) is compared with the total hours from sunrise to sunset (black curve). Fig. 6(B) estimates the DNI, measured in Wm^{-2}, during the reference days for the façade under consideration.

The DNI represents the major part of global irradiance (more than 90%, according to Gao et al. (2018)), and will hereafter be identified with the total input power of the solar eye module, for the sake of simplicity. Irradiance data have been predicted making use of the PVLib Python (Holmgren et al., 2023) and the Ineichen and Perez clear sky model (Ineichen and Perez, 2002; Perez et al., 2002). Comparing the results shown in Figs. 6(A,B) one realizes that the examined façade may exhibit the maximum solar energy harvesting potential at the equinoxes, rather than at the solstices (in clear sky conditions), due to the fact that at the equinoxes it is illuminated by the sun for a considerably larger number of hours, as compared to the solstices, and also due to the observation that the hourly variation of the DNI does not change much in relation to the examined days. We will return to this point later on in the present section.

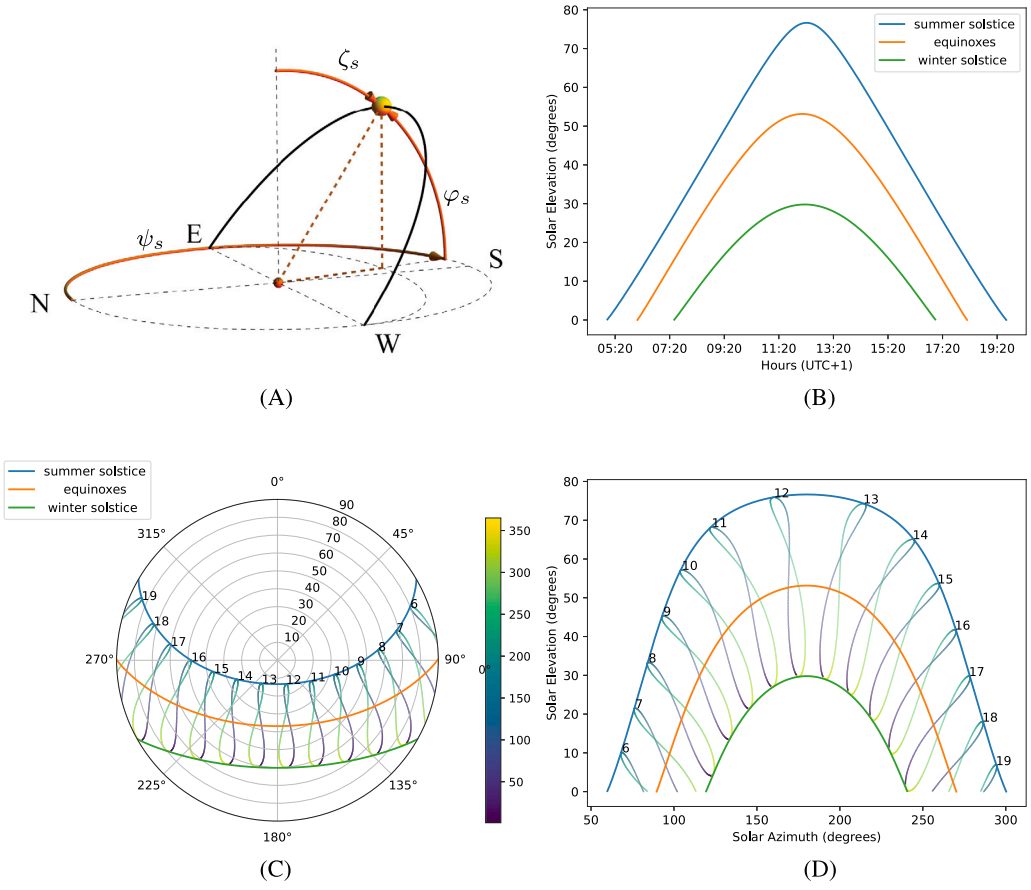

Fig. 5. Predictions of the sun path in Tunis (Tunisia) during solstices and equinoxes of the year 2023 (summer solstice: June 21; winter solstice: December 21; spring equinox: March 20; autumn equinox: September 23). (A) Graphical illustration of azimuth (ψ_s), elevation (φ_s), and zenith angles (ζ_s). (B) Solar elevation versus time on the examined days. (C) Polar plot shows the hourly variations of solar zenith (angular coordinate) and azimuth (radial variable). (D) Solar elevation vs azimuth in Cartesian coordinates. The colored lines in panels (B) to (D) show single-day sun paths for the summer solstice (blue curve), the winter solstice (green curve), and the equinoxes (orange curve). The results for the spring and autumn equinoxes are coincident in these panels. Solar analemmas are included in panels (C) and (D), making use of a color bar indicating the days of the year. (For interpretation of the references to color in this figure legend, the reader is referred to the web version of this article.)

We estimate the input power $P_{b,in}^{\triangle_i}$ on the ith single micro-triangle $\triangle_i$ of the solar eye module through the following equation (Islahi et al., 2015; Gao et al., 2018)

$$P_{b,in}^{\triangle_i} = I_{b,n} \cos\gamma_i \, S_b^i \,, \tag{12}$$

where $I_{b,n}$ indicates the DNI, S_b^i is the total direct-beam-illuminated area of the PV panel lying on $\triangle_i$, and γ_i is the angle between the normal $\mathbf{n}_i$ to $\triangle_i$ and the incident direction of the sunlight. The latter is identified by the unit vector $\mathbf{n}_s$, as shown in Fig. 7(A). In the sequel, we opt to use the indices b and n to indicate 'beam' (i.e., the sun ray beam) and 'normal'. The kinematic study presented in Section 4 leads us to identify that the components of $\mathbf{n}_i$ are scalar functions of the primary folding variable ξ and the tilting angle θ_i of the ith micro-triangle ($i = 1, \dots, 8$), which can be computed using Eqs. (1) to (4) and (11). For what concerns $\mathbf{n}_s$, we use the formula Fig. 5(A)

$$\mathbf{n}_s = \begin{pmatrix} -\cos\varphi_s \cos\psi_s \\ \cos\varphi_s \sin\psi_s \\ \sin\varphi_s \end{pmatrix} \tag{13}$$

and make use of the predictions given in Fig. 5(B) to (D) to estimate the azimuth (ψ_s), elevation (φ_s), and zenith (ζ_s) angles at the Tunis site on the examined days. The quantity $\cos\gamma_i$, which appears in Eq. (12), is computed as follows

$$\cos\gamma_i = \mathbf{n}_i \cdot \mathbf{n}_s \,. \tag{14}$$

As anticipated, we are assuming that each of the eight micro-triangles forming the solar eye module is covered by a custom-made PV array (cf. Section 2). Referring to the geometry shown in Fig. 1(C), and taking into account the edge trims needed to accommodate a PV cell on the $i$the micro-triangle angle $\triangle_i$, we assume that the direct-beam-illuminated area $S_b^i = S_b$ of each micro-triangle is equal to 6528 mm^2. It is worth remarking that the angle γ_i between $\mathbf{n}_i$ and $\mathbf{n}_s$ is zero only if the unit vectors are collinear and point towards the sun. Due to the nature of the kinematics of the solar eye reported in Section 4, it is easily shown that it is not possible to achieve such a condition at the same time for all the micro-triangles composing the system. We are therefore led to study the following maximization problem, with the aim of predicting an optimized value of the overall solar input power of the solar eye module

$$P_{in} = \sum_{i=1}^{8} P_{b,in}^{\triangle_i} = I_{b,n} \, S_b \sum_{i=1}^{8} \max\left(0, \cos\gamma_i\right), \tag{15}$$

under the constraints $0 \le \xi \le 1$ and $0° \le \theta_i \le 94°$ ($0\,\text{rad} \le \theta_i \le 1.64\,\text{rad}$), $i = 1, \dots, 8$. We solve problem (15) making use of the function `NMaximize` of *Mathematica*®13.2 (using the options: `MaxIterations` = 1000, `AccuracyGoal` = 15, and `PrecisionGoal` = 14), by updating the configuration of the solar eye 20 times per hour (an adjustment every three minutes), during the lighting time on the examined days at the Tunis site. This means that we solve problem (15) repeatedly along a discretization in time steps of 180 s of the hours of sunlight. At each step we assume the results of the previous step for the vector variable $\mathbf{z} = \{\xi, \theta_1, \dots, \theta_8\}$ as an initial guess of the maximization algorithm.

The time variation of the optimal value of P_{in} is shown in Fig. 7(B) to (C), with reference to the winter solstice (Panel (B)), the equinoxes

Table 1
Selected results of the optimization problem (15) during the daytime hours of the Winter solstice at the Tunis site.

Hour UTC+1	DNI Wm^{-2}	P_{in} W	ξ –	θ_1 rad	θ_2 rad	θ_3 rad	θ_4 rad	θ_5 rad	θ_6 rad	θ_7 rad	θ_8 rad
7.33	2.57	0.09	0.41	0.70	0.	1.64	0.69	0.70	1.64	0.	0.7
8.33	391.77	16.20	0.39	0.44	0.	1.52	0.24	1.07	1.59	0.	0.86
9.33	633.08	28.31	0.28	0.11	0.	1.13	0.	0.96	1.22	0.	0.83
10.33	736.59	34.62	0.21	0.	0.	0.80	0.	0.88	0.86	0.	0.82
11.33	780.29	37.42	0.19	0.	0.13	0.51	0.	0.85	0.54	0.10	0.83
12.33	787.82	37.90	0.19	0.	0.39	0.26	0.	0.84	0.24	0.40	0.85
13.33	762.67	36.30	0.19	0.	0.65	0.	0.	0.81	0.	0.70	0.85
14.33	692.52	31.83	0.24	0.	0.96	0.	0.	0.82	0.	1.04	0.91
15.33	532.79	22.94	0.34	0.11	1.33	0.	0.28	0.86	0.	1.42	1.03
16.33	156.71	6.15	0.41	0.41	1.64	0.	0.58	0.80	0.	1.64	0.97

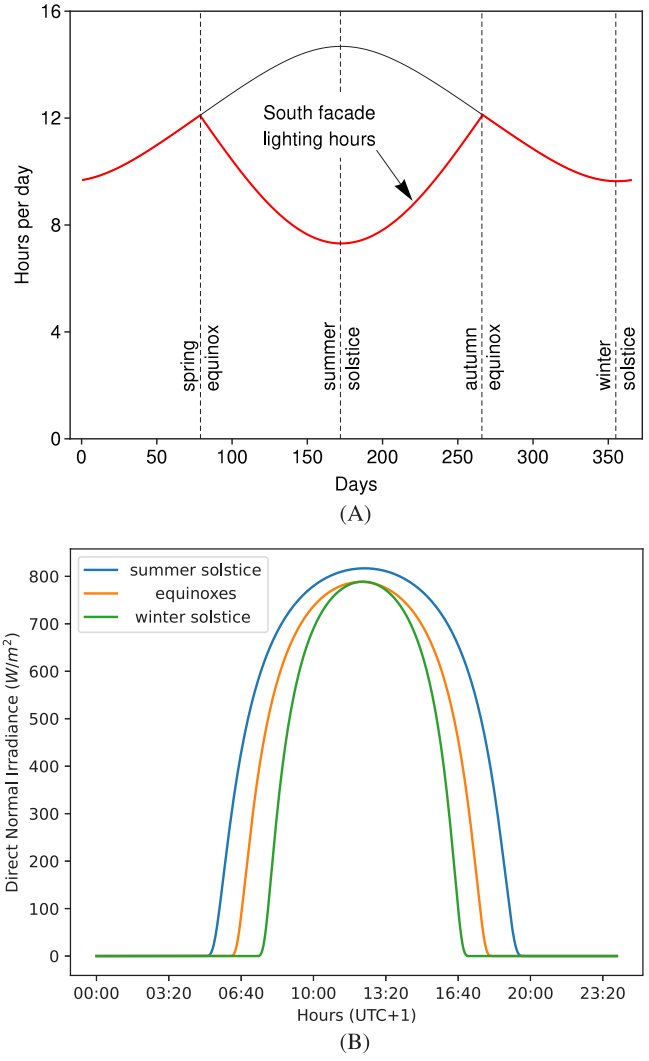

Fig. 6. (A) Predicted number of hours per day a south facing façade is illuminated by the sun in the city of Tunis, 2023. (B) Daily variation of direct normal irradiance, measured in Wm^{-2}, during the reference days. Hours are measured in local time, UTC+01:00. (For interpretation of the references to color in this figure legend, the reader is referred to the web version of this article.)

(Panel (C): one obtains identical results for the spring and autumn equinoxes, cf. Fig. 6) and the summer solstice (Panel (C)). Selected numerical results are listed in Table 1 (winter solstice), Table 2 (equinoxes) and Table 3 (summer solstice), considering one sample per hour during daytime.

The output electrical power is given by the equation

$$P_{out} = P_{in}\eta \tag{16}$$

where η indicates the power conversion efficiency (PCE) of the employed solar cells. The integrals of P_{in} and P_{out} over a given time interval provide the corresponding values of the input solar energy E_{in} and the output electrical energy $E_{PV,m}$ harvested by the solar eye solar module, respectively. We assume that the PCE declared by FuturaSun® for their Silk® Nova Red cells is the one used in the PV array of our solar eye module, that is: $\eta = 18.97\%$ (FuturaSun®, 2024). Figs. 7(B) to (D) show the hourly variations of P_{out} (red curves) and the values of $E_{PV,m}$ computed over 24 h (red shaded regions) for the examined days at the Tunis site. Selected values of E_{in} and $E_{PV,m}$ are provided in Table 4. Four configurations of the solar eye module, which maximize P_{out} through the solution of problem (15), are shown in Fig. 8 in relation to the autumn equinox, which proved to be a day offering the absolute maximum value of $E_{PV,m}$ among the days considered in the present study (together with the spring equinox). The results illustrated in Fig. 8 highlight that the micro-triangles forming the solar module exhibit different normal vectors in relation to the optimal configuration of the solar eye module.

The ability of the solar eye to harvest solar energy is influenced by different factors, in particular, the location of the site where the system is installed plays a key role. The study of the solar irradiation of the Tunis site, presented in Figs. 5–6, reveals that the lighting time of a south-facing vertical surface in Tunis does not necessarily coincide with the sunrise to the sunset time interval. During the time window between the spring and autumn equinoxes, the results shown in Fig. 5(A) indeed point out that the above lighting time does not coincide with the overall interval of lighting hours at the Tunis site, since this surface is not directly illuminated during part of the day. This inconvenience worsens at latitudes further south than Tunis. We present in Supplementary Materials a study on the solar energy harvesting capacity of a solar eye module placed on a south-facing surface of a building located in Jeddah, Saudi Arabia, positioned at 21.492 506 085 latitude and 39.177 577 234 longitude (see Figs. S1–S2 of Supplementary Text). This study leads us to the results listed in Table 5. By comparing the results of Tables 4 and 5, we realize that the solar eye module in Jeddah has greater energy harvesting capacity at the winter solstice and lower energy harvesting capacity at the equinoxes, as compared to the same module in Tunis. Table 5 also shows that the solar eye module has zero energy harvesting capacity at the summer solstice in Jeddah. As a matter of fact, on such a day and during the entire period May 26–July 16, 2023, the solar eye is shaded during the entire time interval from sunrise to sunset at this site (see Supplementary Materials for further details).

The energy production estimations presented above have been obtained by assuming that the primary and the secondary folding motion systems ensure the best sun tracking of all the PV triangles, with all the cells operating at their Maximum Power Point (MPP). The electrical connection among the cells has not been accounted for. It is well known (Petrone et al., 2017) that, if the cells are electrically connected in series, possible mismatches give rise to power drops, which are usually mitigated by the use of bypass diodes. As it is shown in Fig. 1, the system designed to allow the transition from the open to the close

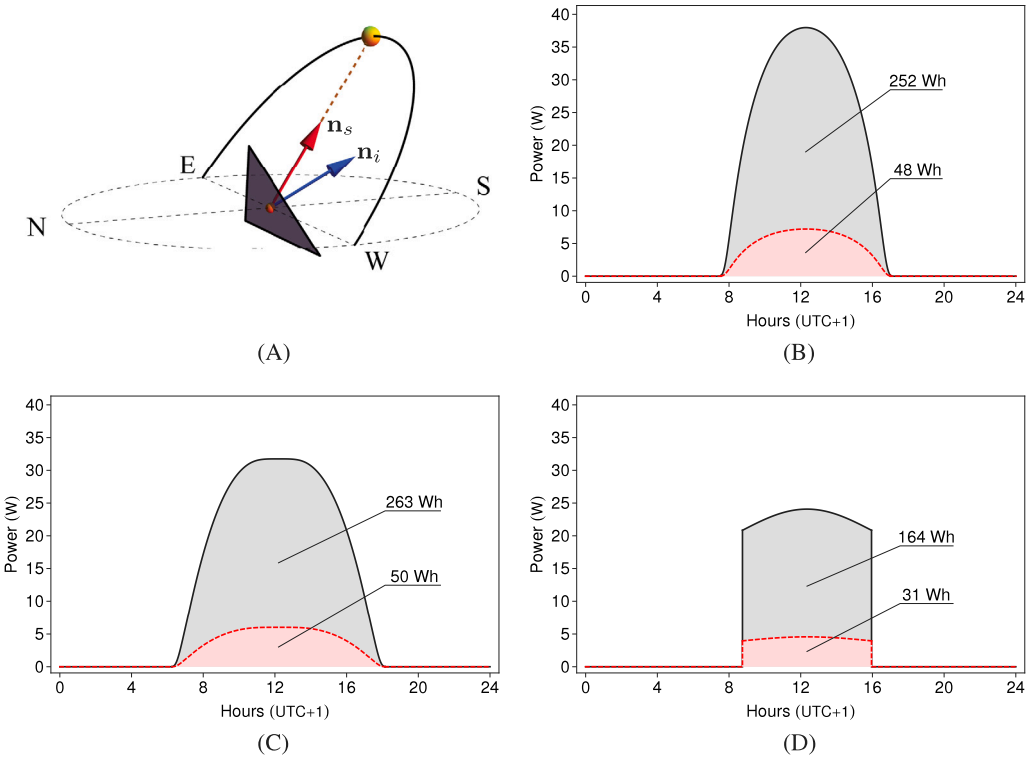

Fig. 7. (A) Illustration of the unit normal vector of the generic panel and the unit vector aligned with the sun rays. (B-D) Hourly variations of the optimal value of the total solar power input on the solar eye module (black lines) and the harvested power output (dashed red lines), measured in W, during the reference days at the Tunis site: winter solstice (B), equinoxes (C) and summer solstice (D). Hours are in local time (UTC+01:00). Shaded areas represent input and output energies, measured in W h. (For interpretation of the references to color in this figure legend, the reader is referred to the web version of this article.)

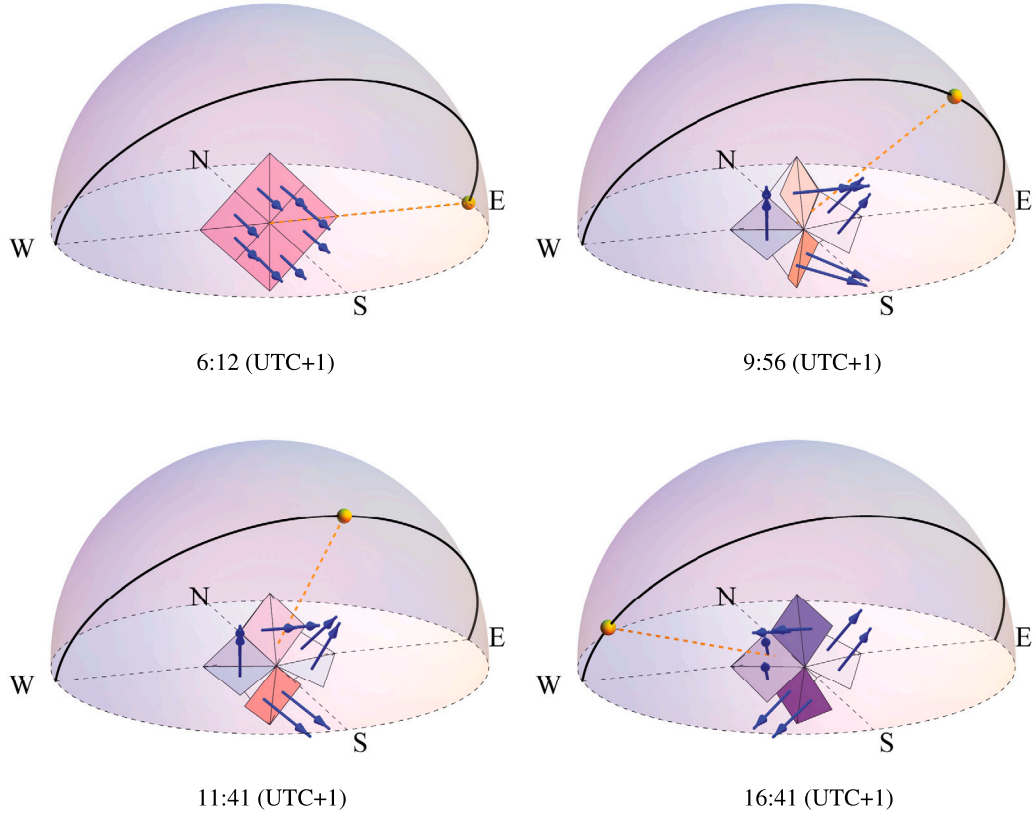

Fig. 8. Configurations of the solar eye module at four different hours of the autumn equinox. The sun path and the sun position are shown, together with the sun ray direction (dashed yellow line) and the normal vectors to the micro-triangles (blue arrows). The fully flat configuration at 6:12 (UTC+1) is taken as reference. (For interpretation of the references to color in this figure legend, the reader is referred to the web version of this article.)

Table 2
Selected results of the optimization problem (15) during the daytime hours of the Equinoxes at the Tunis site.

Hour UTC+1	DNI Wm^{-2}	P_{in} W	ξ –	θ_1 rad	θ_2 rad	θ_3 rad	θ_4 rad	θ_5 rad	θ_6 rad	θ_7 rad	θ_8 rad
6.12	0.16	0.	0.	0.	0.	0.	0.	0.	0.	0.	0.
7.12	298.60	8.53	0.66	0.74	0.	1.64	0.	0.31	1.64	0.	1.41
8.11	556.74	18.24	0.57	0.38	0.	1.64	0.	0.32	1.64	0.	1.52
9.11	682.08	26.33	0.44	0.	0.	1.62	0.	1.64	1.64	0.	1.48
10.11	746.81	30.26	0.43	0.	0.11	1.34	0.	1.64	1.64	0.	1.54
11.12	778.68	31.63	0.42	0.	0.39	1.02	0.	1.64	1.38	0.03	1.59
12.12	788.28	31.74	0.40	0.	0.67	0.67	0.	1.62	0.67	0.68	1.62
13.12	778.41	31.63	0.42	0.	1.02	0.38	0.	1.59	0.02	1.38	1.64
14.12	746.18	30.24	0.43	0.	1.34	0.11	0.	1.54	0.	1.64	1.64
15.12	680.83	26.29	0.44	0.	1.62	0.	0.01	1.47	0.	1.64	1.64
16.12	554.16	19.08	0.46	0.	1.64	0.	0.16	1.38	0.	1.64	1.64
17.12	292.88	8.25	0.50	0.	1.64	0.	0.44	1.23	0.	1.64	1.64

Table 3
Selected results of the optimization problem (15) during the daytime hours of the Summer solstice at the Tunis site.

Hour UTC+1	DNI Wm^{-2}	P_{in} W	ξ –	θ_1 rad	θ_2 rad	θ_3 rad	θ_4 rad	θ_5 rad	θ_6 rad	θ_7 rad	θ_8 rad
5.06	0.19	0.	0.	0.	0.	0.	0.	0.	0.	0.	0.
6.06	258.13	0.	0.	0.	0.	0.	0.	0.	0.	0.	0.
7.06	522.76	0.	0.	0.	0.	0.	0.	0.	0.	0.	0.
8.06	661.68	0.	0.	0.	0.	0.	0.	0.	0.	0.	0.
9.06	738.79	20.91	0.99	0.62	0.66	1.64	0.	1.05	0.71	0.	1.64
10.06	783.03	22.68	0.99	0.49	0.93	1.64	0.	0.81	0.34	0.	1.64
11.06	807.06	22.75	0.99	0.35	1.21	1.64	0.	0.93	0.73	0.	1.64
12.06	816.53	24.57	0.61	0.	0.91	1.10	0.	1.64	0.07	0.07	1.64
13.06	813.45	24.44	0.61	0.	1.29	0.73	0.	1.64	0.	0.81	1.64
14.06	797.17	23.84	0.63	0.	1.64	0.41	0.	1.64	0.	0.72	1.64
15.06	764.12	21.55	0.62	0.	1.64	0.07	0.	1.64	0.	0.34	1.64
16.06	705.80	0.	0.	0.	0.	0.	0.	0.	0.	0.	0.
17.06	603.26	0.	0.	0.	0.	0.	0.	0.	0.	0.	0.
18.06	412.30	0.	0.	0.	0.	0.	0.	0.	0.	0.	0.
19.06	77.30	0.	0.	0.	0.	0.	0.	0.	0.	0.	0.

Table 4
Values of the input energy E_{in} and harvested (output) energy $E_{PV,m}$ during 24 h on the examined days at the Tunis site.

Reference day	E_{in} (W h)	$E_{PV,m}$ (W h)
Winter solstice	251.864	47.779
Equinoxes	261.657	49.636
Summer solstice	165.071	31.314

Table 5
Values of the input energy E_{in} and harvested (output) energy $E_{PV,m}$ during 24 h on the examined days at the Jeddah site.

Reference day	E_{in} (W h)	$E_{PV,m}$ (W h)
Winter solstice	288.347	54.699
Equinoxes	249.664	47.361
Summer solstice	0.	0.

positions, and vice versa, of the solar eye, ensures that the eight triangles do not move independently. Indeed, they form four couples of triangles, each couple always keeping the same orientation towards the sun. This means that the cells in each couple of triangles always operate in the same conditions and they can be electrically connected in series without experiencing any power drop in whichever position the solar eye takes. This suggests a further optimization study about the electrical connection among the cells in the window, in order to optimize the electrical topology to achieve the maximum energy harvesting. A possible solution to investigate in future work might be the one simulated in Orozco-Gutierrez et al. (2019) or the adoption of power optimizers, as it is widely discussed in Femia et al. (2013).

5.2. Required activation energies

We measured the electric powers required to activate the primary and secondary folding motion of the solar eye through experimental measurements performed on the physical model described in Section 2. We used a digital multimeter Nimex NI-2100 to measure the activation currents of the employed DC motors. The multiplication of such values by the supply voltage of 12 V gave us instantaneous values of the activation powers, as shown in Figs. 9(A,B).

For what concerns the primary folding motion, we measured the power $P_{act,1}$ required by the competent DC motor during the complete folding and unfolding motion of one macro-triangle forming the solar eye. Such a motion was parameterized through the variable $\xi \in [0, 1]$ introduced in Section 4, which is equal to zero in the fully flat configuration of the generic macro-triangle, and is equal to 1 in the fully folded configuration. The instantaneous variation of $P_{act,1}$ with ξ, together with the experimentally observed average value $\bar{P}_{act,1} = 865$ mW is illustrated in Fig. 9(A). The time needed to let ξ grow from 0 to 1 was equal to 30 s (primary folding time), approximately (average time step of the measurements: 0.58 s), from which the activation velocity $\dot{\xi}$ is computed.

The electric power $P_{act,2}$ needed by the employed DC motor to activate the secondary folding motion was also measured, by letting the tilting angle θ of the generic micro-triangle vary between 0° and 94°. We obtained in this way the curve illustrated in Fig. 9(B), which shows the instantaneous values measured for $P_{act,2}$ and the average value $\bar{P}_{act,2} = 755$ mW. The time needed to let θ grow from 0° to 94° was equal to 20 s (secondary folding time), approximately (average time step: 0.58 s), from which the activation velocity $\dot{\theta}$ is computed.

We can use the above experimental data to estimate the activation energy requested by the sun tracking strategy illustrated in Section 5.1. Let us consider a discretization into time steps of $\Delta t = 180$ s each of the sunlight hours. With reference to the generic step, the optimization problem (15) returns the values at the initial time t and the final time $t + \Delta t$ of the variable $\mathbf{z} = \{\xi, \theta_1, \ldots, \theta_8\}$. The incremental activation energy required in this step is estimated to make use of the approximate

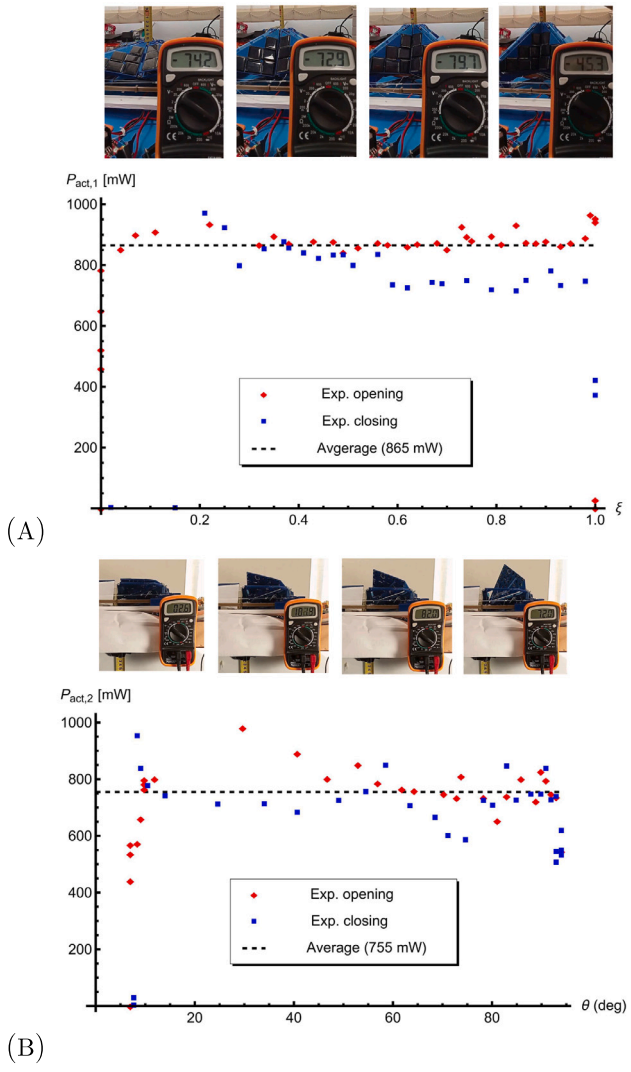

Fig. 9. Curves of the demanded electric powers experimentally measured for the primary and secondary folding motions of the solar eye. (A) Electric power $P_{act,1}$ needed to activate the primary folding motion of the overall solar eye vs. the opening variable ξ. (B) Electric power $P_{act,2}$ needed to activate the secondary folding motion of a single micro-triangle vs. the tilting angle θ. The insets show snapshots extracted from the videos of the experimental tests. The digital multimeters shown in the snapshots measure the activation current in mA, which multiplied by the supply voltage of 12 V gives the activation power in mW.

formula

$$\Delta E_{act} \approx \frac{|\xi(t) - \xi(t - \Delta t)|}{\dot{\xi}} \bar{P}_{act,1} + \sum_{i=1}^{8} \frac{|\theta_i(t) - \theta_i(t - \Delta t)|}{\dot{\theta}_i} \bar{P}_{act,2} \qquad (17)$$

where $\dot{\xi}$ and $\dot{\theta}_i$ are the activation speeds assumed equal to the values obtained in the above experimental tests. Table 6 shows the overall activation energies E_{act} that are needed to perform the sun-tracking strategy of a solar eye module in the examined days for the Tunis site. The same table also reports the total times $T_{act,1}$ and $T_{act,2}$ spent for the primary and secondary folding, respectively, and the ratio between E_{act} and the total harvested energy $E_{PV,m}$ of a solar eye module. One observes that such a ratio is considerably lower than one, and assumes mean values varying from nearly 1.5‰ (1.5/1000) up to about 5‰. This result is explained by the observation that the electric energy produced by the cells, when optimally oriented, is only minimally consumed to fold the micro-triangles, due to the employment of a low-energy consumption actuation strategy, and the short intervals of time during which the system moves.

Table 6
Overall activation energies required and ratios between required and harvested energies on the reference days for the Tunis site.

Reference day	$T_{act,1}$	$T_{act,2}$	E_{act}	$E_{act}/E_{PV,m}$
–	s	s	W h	–
Winter solstice	39.052	282.928	0.069	1.438‰
Equinoxes	65.049	526.368	0.126	2.539‰
Summer solstice	62.078	666.595	0.155	4.941‰

5.3. Net produced electrical energies

Using the results presented in Tables 4 and 6, and taking into account that the TMas window shown in Fig. 2 incorporates 64 solar eye modules, we conclude that such an element is able to produce net electrical energies E_{TW} that are approximately equal to 3.05 kW h, 3.17 kW h and 1.99 kW h during the winter solstice, the equinoxes and the summer solstice, respectively. Such rough estimates assume, for the sake of simplicity, that all the solar eye modules exhibit the same solar energy harvesting capacity. According to recent statistics (Enerdata, 2024), the per capita electricity consumption in Tunisia is 1500 kW h/year. Thus, the daily consumption of a four-person family can be estimated at close to 16 kW h. Consequently, a single TMas window can provide more than 10% of the daily electrical energy needs of the family (percentage varying from the 12% of the summer solstice to the 20% of the winter solstice and equinoxes). Such an estimate will be refined in a future study by also accounting for the effects of the electrical connections among the cells and of the electronic power processing circuits.

6. Concluding remarks

We have presented the design of a Mashrabiya window, which employs tessellations of origami solar eye modules with tensegrity architecture. These modules incorporate foldable PV panels that can be oriented by optimized sun-tracking mechanisms, in order to maximize the direct normal irradiation on each PV string. The presented study has shown that the analyzed solar modules require very limited energy to activate the sun-tracking mechanism, thanks to the adoption of folding motions simply controlled by changing the rest lengths of the activation cables. As a result, the designed Mashrabiya elements offer positive-energy solutions for energy efficient buildings, coupling solar energy harvesting capacity with appealing aesthetic features. They provide energy-efficient reformulations of traditional Mashrabiya systems, and can be also conveniently employed to design dynamic solar façades.

A quite encouraging estimation of the electrical energy production has been achieved, despite not being able to include the effect of the electrical connection among the cells and of the power processing system for supplying the load. By considering the example of a four-person family living in Tunisia, it has been determined that a single window is able to provide, on average, at least the 10% of the electrical energy needs. At lower latitudes, an improved energy production is expected at the winter solstice, with a worse result at the summer solstice, when considering a vertical window oriented towards the south. In a Mediterranean context as well as in a more tropical one, the Mashrabiya window can effectively contribute to reducing energy usage from the electrical distribution grid, thus helping to achieve the goal of having a Near Zero Energy Building (NZEB), and to improve the comfort of the residents through a proper use of the produced energy. The value of the harvested energy cumulates appreciably in the case where the window is installed in a house in a rural area with no connection to the electrical grid.

Future extensions of the present study will analyze the design of solar façades with Mashrabiya architecture (ArchDaily, 2012), as well as PV greenhouses that are based on the solar eye modules studied in this work and OPV cells (Gorjian et al., 2022; Lu et al., 2022; Fernández et al., 2022; Moshari et al., 2023). An additional line of future research will deepen the study initiated in this work on the solar energy harvesting capacity of PV-equipped Mashrabiyas, with the aim of optimizing the coordination between the sun-tracking algorithms of the modules forming the system, and the electric connections among the PV cells. The possible reuse of the components of such systems, their life cycle analysis, and the inclusion of green materials and activation cables made of shape memory alloys in the solar eye modules will also be investigated in future studies (Fraternali and de Castro Motta, 2023).

Funding

This research has been funded under the National Recovery and Resilience Plan (NRRP), by the European Union - NextGenerationEU, within the project with grant number P2022CR8AJ (F.F. PI: "Ricerca finanziata dall'Unione Europea - Next Generation EU"). This research has also been funded by the NextGenerationEU PRIN2022 research project with grant number 20224LBXMZ (F.F. PI). F.F. and R.N.C. also acknowledge the support by the Italian Ministry of Foreign Affairs and International Cooperation within the Italy-USA Science and Technology Cooperation Program 2023–2025, Project "Next-generation green structures for natural disaster-proof buildings" (grant n. US23GR15).

CRediT authorship contribution statement

Fernando Fraternali: Conceptualization, Funding acquisition, Investigation, Methodology, Project administration, Supervision, Writing – original draft, Writing – review & editing, Formal analysis, Validation, Visualization, Resources. **Enrico Babilio:** Conceptualization, Data curation, Formal analysis, Investigation, Software, Supervision, Validation, Writing – original draft, Writing – review & editing, Methodology. **Rana Nazifi Charandabi:** Conceptualization, Data curation, Methodology, Software, Validation, Writing – original draft, Writing – review & editing, Resources. **Giovanni Germano:** Investigation, Methodology, Resources, Validation, Writing – original draft, Writing – review & editing. **Raimondo Luciano:** Conceptualization, Formal analysis, Investigation, Methodology, Supervision, Validation, Writing – original draft, Writing – review & editing. **Giovanni Spagnuolo:** Conceptualization, Formal analysis, Methodology, Supervision, Validation, Visualization, Writing – original draft, Writing – review & editing.

Declaration of competing interest

The authors declare that they have no known competing financial interests or personal relationships that could have appeared to influence the work reported in this paper.

Data availability

Data will be made available on request.

Appendix A. Supplementary data

Supplementary material related to this article can be found online at https://doi.org/10.1016/j.apples.2024.100190.

References

ArchDaily, 2012. The Mashrabiya house. (ISSN: 0719-8884) https://www.archdaily.com/175582/the-mashrabiya-house-senan-abdelqader. (Accessed 10 April 2024)].

Attoye, D.E., Aoul, K.A.T., Hassan, A., 2017. A review on building integrated photovoltaic façade customization potentials. Sustainability (ISSN: 20711050) 9 (12), 2287. http://dx.doi.org/10.3390/su9122287.

Babilio, E., Miranda, R., Fraternali, F., 2019. On the kinematics and actuation of dynamic sunscreens with tensegrity architecture. Front. Mater. (ISSN: 2296-8016) 6, http://dx.doi.org/10.3389/fmats.2019.00007.

Bonner, J.F., 2016. The historical significance of the geometric designs in the Northeast dome chamber of the friday mosque at Isfahan. Nexus Netw. J. 18 (1), 55–103.

Burgues-Ceballos, I., Lucera, L., Tiwana, P., Ocytko, K., Tan, L.W., Kowalski, S., Snow, J., Pron, A., Bürckstümmer, H., Blouin, N., et al., 2021. Transparent organic photovoltaics: A strategic niche to advance commercialization. Joule 5 (9), 2261–2272.

Ebert, M., Mittag, M., Fellmeth, T., Spribille, A., Mindehoud, T., Gijzen, G., Fath, K.-R., Hecker, R., Eitner, U., 2016. Mosaic modules for improved design options in building integrated photovoltaic modules.

Enerdata, 2024. Enerdata coloured photovoltaic panels. Accessed 10 April 2024.

Fathy, H., 1986. Natural energy and vernacular architecture: principles and examples with reference to hot arid climates. p. 172, xxiii.

Femia, N., Petrone, G., Spagnuolo, G., Vitelli, M., 2013. Power Electronics and Control Techniques for Maximum Energy Harvesting in Photovoltaic Systems. CRC Press.

Fernández, E.F., Villar-Fernández, A., Montes-Romero, J., Ruiz-Torres, L., Rodrigo, P.M., Manzaneda, A.J., Almonacid, F., 2022. Global energy assessment of the potential of photovoltaics for greenhouse farming. Appl. Energy 309, 118474. http://dx.doi.org/10.1016/j.apenergy.2021.118474.

Fraternali, F., de Castro Motta, J., 2023. Mechanics of superelastic tensegrity braces for timber frames equipped with buckling-restrained devices. Int. J. Solids Struct. 281, 112414.

Fraternali, F., de Castro Motta, J., Germano, G., Babilio, E., Amendola, A., 2024. Mechanical response of tensegrity-origami solar modules. Appl. Eng. Sci. 17, 100174. http://dx.doi.org/10.1016/j.apples.2023.100174.

FuturaSun®, 2024. Coloured photovoltaic panels. https://www.futurasun.com/en/products/photovoltaic-monocrystalline-coloured-panels-silk-colour/. (Accessed 10 April 2024).

Gao, Y., Dong, J., Isabella, O., Santbergen, R., Tan, H., Zeman, M., Zhang, G., 2018. A photovoltaic window with sun-tracking shading elements towards maximum power generation and non-glare daylighting. Appl. Energy 228, 1454–1472. http://dx.doi.org/10.1016/j.apenergy.2018.07.015.

Giovannini, L., Verso, V.R.L., Karamata, B., Andersen, M., 2015. Lighting and energy performance of an adaptive shading and daylighting system for arid climates. Energy Procedia 78, 370–375. http://dx.doi.org/10.1016/j.egypro.2015.11.675.

Gorjian, S., Bousi, E., Özdemir, Ö.E., Trommsdorff, M., Kumar, N.M., Anand, A., Kant, K., Chopra, S.S., 2022. Progress and challenges of crop production and electricity generation in agrivoltaic systems using semi-transparent photovoltaic technology. Renew. Sustain. Energy Rev. 158, 112126. http://dx.doi.org/10.1016/j.rser.2022.112126.

Holmgren, W., Anderson, K., Hansen, C., robwandrews, Mikofski, M., Jensen, A.R., Lorenzo, A., Krien, U., bmu, Driesse, A., Stark, C., DaCoEx, de León Peque, M.S., Transue, T., Luis, E., kt, Priyadarshi, N., mayudong, Heliolytics, Miller, E., Anoma, M.A., Guo, V., Boeman, L., Stein, J., Aneja, S., Vining, W., jforbess, Lunel, T., Leroy, C., Morgan, A., 2023. Pvlib/pvlib-python: v0.10.3. http://dx.doi.org/10.5281/zenodo.10412885.

Ineichen, P., Perez, R., 2002. A new airmass independent formulation for the Linke turbidity coefficient. Sol. Energy (ISSN: 0038-092X) 73 (3), 151–157. http://dx.doi.org/10.1016/S0038-092X(02)00045-2.

Islahi, A., Shakil, S., Hamed, M., 2015. Hottel's clear day model for a typical arid city-Jeddah. Int. J. Eng. Sci. Invent. 4 (6), 32–37.

Karamata, B., Andersen, M., 2014. Concept, design and performance of a shape variable mashrabiya as a shading and daylighting system for arid climates. In: 30th PLEA Conference-Sustainable Habitat for Developing Societies. Vol. 2, CEPT University Ahmedabad, pp. 344–351, CONF.

Lu, L., Effendy Ya'acob, M., Shamsul Anuar, M., Nazim Mohtar, M., 2022. Comprehensive review on the application of inorganic and organic photovoltaics as greenhouse shading materials. Sustain. Energy Technol. Assess. 52, 102077. http://dx.doi.org/10.1016/j.seta.2022.102077.

Mittag, M., Ebert, M., Wilson, H.-R., Fellmeth, T., 2018. Mosaic module concept for cost-efficient and aesthetic BIPV modules. http://dx.doi.org/10.4229/35thEUPVSEC20182018-6AO.7.5.

Moshari, A., Aslani, A., Entezari, A., Ghanbari, K., 2023. Performance assessment of the integration of semitransparent solar cells with different geometry of greenhouses under different climate regions. Environ. Sci. Pollut. Res. 30 (22), 62281–62294.

Orozco-Gutierrez, M., Spagnuolo, G., Ramos-Paja, C., Ramirez-Scarpetta, J., Ospina-Agudelo, B., 2019. Enhanced simulation of total cross tied photovoltaic arrays. Math. Comput. Simulation (ISSN: 0378-4754) 158, 49–64. http://dx.doi.org/10.1016/j.matcom.2018.05.016, ELECTRIMACS 2017, The International Conference on Modeling and Simulation of Electric Machines, Converters and Systems (IMACS TC 1).

Perez, R., Ineichen, P., Moore, K., Kmiecik, M., Chain, C., George, R., Vignola, F., 2002. A new operational model for satellite-derived irradiances: description and validation. Sol. Energy (ISSN: 0038-092X) 73 (5), 307–317. http://dx.doi.org/10.1016/S0038-092X(02)00122-6.

Petrone, G., Ramos-Paja, C., Spagnuolo, G., 2017. Photovoltaic Sources Modeling. Wiley-IEEE Press.

Song, W., Ge, J., Xie, L., Chen, Z., Ye, Q., Sun, D., Shi, J., Tong, X., Zhang, X., Ge, Z., 2023. Semi-transparent organic photovoltaics for agrivoltaic applications. Nano Energy 116, 108805. http://dx.doi.org/10.1016/j.nanoen.2023.108805.

Taki, A., Kumari, H., 2023. Examining Mashrabiya's impact on energy efficiency and cultural aspects in Saudi Arabia. Sustainability 15 (13), http://dx.doi.org/10.3390/su151310131.

Vassiliades, C., Agathokleous, R., Barone, G., Forzano, C., Giuzio, G.F., Palombo, A., Buonomano, A., Kalogirou, S., 2022. Building integration of active solar energy systems: A review of geometrical and architectural characteristics. Renew. Sustain. Energy Rev. (ISSN: 18790690) 164, 112482. http://dx.doi.org/10.1016/j.rser.2022.112482.